

Microquasar Remnants as Pevatrons Illuminating the Galactic Cosmic Ray Knee

Bing Theodore Zhang^{1,2*}

¹ Key Laboratory of Particle Astrophysics and Experimental Physics Division and Computing Center, Institute of High Energy Physics, Chinese Academy of Sciences, 100049 Beijing, China and

² TIANFU Cosmic Ray Research Center, Chengdu, Sichuan, China

Shiqi Yu[†]

Department of Physics and Astronomy, University of Utah, Salt Lake City, Utah, USA

(Dated: February 10, 2026)

Microquasars are primary candidates for Galactic PeVatrons, yet their collective contribution to the cosmic ray (CR) “knee” remains poorly understood. We investigate this contribution by simulating anisotropic diffusive propagation through the Galactic magnetic field (GMF). Our results demonstrate that the GMF establishes a transport regime where magnetic connectivity between sources and the solar neighborhood determines the local flux. Active sources aligned with local GMF lines, such as Cygnus X-1, exhibit significant flux enhancements, while magnetically disconnected sources, such as V616 Mon, are strongly suppressed. By integrating source evolution with anisotropic transport, we show that the observed proton bump at the CR “knee” is best reproduced by the cumulative contribution of microquasar remnants, which is often dominated by a few nearby or recent events, rather than the active ones alone. We find that a harder injection spectrum allows CRs from remnants to reproduce the PeV bump feature after propagation, as low-energy CRs have sufficient time to accumulate while high-energy CRs escape the Galactic plane. Our findings suggest that the integrated history of microquasar remnants, governed by the interplay of source age and magnetic connectivity, is the primary driver populating the observed CR “knee”.

Introduction— Recent observations by the LHAASO collaboration have identified a prominent “bump” in the cosmic ray (CR) proton spectrum from 100 TeV to 30 PeV [1], which is coincident with the position of the “knee” of the all-particle spectrum [2]. This spectral feature necessitates a distinct population of Galactic PeVatrons [3], suggesting that the observed CR is not a featureless power-law spectrum but is shaped by specific accelerator classes [e.g., 4–11]. Our previous work has established the physical foundations for microquasars as primary PeVatron candidates, demonstrating that shear acceleration within jet-cocoon systems can theoretically produce the cosmic-ray flux required to account for the observed spectral “bump” [4]. However, the Galactic magnetic field (GMF) channels CRs preferentially along field lines, giving rise to anisotropic diffusion that modifies the observed CR spectra non-negligibly [12–14]. This magnetic channeling implies that two equidistant sources may yield vastly different observed fluxes depending on their connectivity to the solar neighborhood.

In this paper, we extend our previously established CR model [4] by incorporating detailed propagation through the GMF. We evaluate the observed CR spectra by accounting for the cumulative contributions of both active and fossil microquasars, i.e., remnants. We define the latter as systems where the relativistic jet activity has ceased, leaving behind expanding clouds of CRs. Although their central engines are no longer injecting fresh particles, the CRs accelerated during past

active epochs continue to diffuse through the interstellar medium (ISM). Our results demonstrate that the interplay between these populations and GMF transport is essential to reproduce the observed data, and that a hard injection spectrum is favored to meet the energy budget requirement. By building directly upon the hypothesis of microquasars as PeVatrons, this work provides a comprehensive assessment of their collective role in producing the PeV diffuse CRs.

Methodology and Models— We simulate CR propagation using `DiffusiveSDE` module in the `CRPROPA` 3.2 framework. The GMF is represented by the JF12 model [15, 16]. The expected CR flux at Earth is estimated by recording particles entering the observer, a spherical volume of radius 200 pc centered at the solar neighborhood. The observer volume is chosen to be large enough to ensure statistical convergence of the stochastic particles while remaining small relative to Galactic scales, thereby providing a robust estimate of the local CR density.

Since this work focuses on interpreting the time-integrated CR flux, we safely neglect uncertainties arising from jet variability [17] and assume a constant CR injection rate. We further assume that CRs are injected into the ISM immediately after escaping from the sources and neglect the possible effects arising from jet duty cycles [18].

For a source with a time-dependent injection rate $Q(E)$ [erg s⁻¹], the observed particle density $n(E, \mathbf{r}, \tau_{\text{age}})$ at position \mathbf{r} is obtained by integrating the source’s injection history:

$$n(E, \mathbf{r}, \tau_{\text{age}}) = Q(E) \int_{\tau_{\text{min}}}^{\tau_{\text{age}}} \mathcal{P}(\mathbf{r}, E, \tau) d\tau, \quad (1)$$

* zhangbing@ihep.ac.cn

† shiqi.yu@utah.edu

where $\mathcal{P}(\mathbf{r}, E, \tau)$ acts as the probability density function for a particle's position after a propagation time τ . The integration limits are defined by $\tau_{\min} = \max(0, \tau_{\text{age}} - \tau_{\text{dur}})$, where τ_{age} represents the time elapsed since the jet onsets and τ_{dur} is the engine's lifetime. The observed flux is then $J(E) = \frac{c}{4\pi} n(E, \mathbf{r}, \tau_{\text{age}})$.

We adopt the physically motivated “Model A” from our previous work [4] as the injection spectra. This model is characterized by a hard spectral shape with a steep cutoff. For comparison, we also inject from a template of a generic power-law function with a spectral index of 2, a typical choice of diffusive shock acceleration scenario for such sources [7].

The diffusion coefficient parallel to the local magnetic field lines is $D_{\parallel} = 6.1 \times 10^{28} (E/4 \text{ GeV})^{1/3} \text{ cm}^2 \text{ s}^{-1}$ [19]. The perpendicular component is defined as $D_{\perp} = \varepsilon D_{\parallel}$, where the coefficient ε represents the anisotropic diffusion [20]. The choice of ε exerts a direct influence on CR propagation in the Galactic plane. In the local interstellar medium (JF12 model), the turbulence is strong ($\delta B/B_0 \sim 3$). Despite this, the transport remains highly anisotropic ($D_{\parallel} \gg D_{\perp}$). This is because the Larmor radius ($r_L \sim 0.3 \text{ pc}$) for PeV particles is significantly smaller than the correlation length of the turbulence ($L_c \sim 10 - 100 \text{ pc}$), and their effective transverse transport is driven by the field-line random walk of the magnetic flux tubes themselves [21].

Throughout this work, we assume a cylindrical Galactic halo with $R_G = 20 \text{ kpc}$ and $H_G = 2 \text{ kpc}$ as the boundary conditions for CR propagation in the Milky Way.

GMF Effects— To contribute significantly ($\gtrsim 10\%$) to the observed PeV flux, a CR energy density of $\sim (0.4 - 4) \times 10^{-5} \text{ eV cm}^{-3}$ is required [1]. Under the assumption of purely isotropic diffusion, using the method in Ref. [22], we analytically calculate that a single source must be located within $d \lesssim 0.5 \text{ kpc}$ and have an age $\tau_{\text{age}} \lesssim 0.2 \text{ Myr}$ to dominate the local flux (see Appendix A for details). As the distance increases to $d \sim 2 \text{ kpc}$, the contribution to flux drops by approximately 90%.

However, the presence of GMF channels cosmic rays along spiral arms via diffusion anisotropy [23] and makes magnetic connectivity, as a primary driver of the observed local flux. As illustrated in the spatial distribution of 10 PeV CRs in Fig. 1, this creates a filamentary morphology for the CR clouds. For sources at the positions of V616 Mon [24] and XTE J1118+480 [25], the local magnetic field lines do not pass through the solar neighborhood. With inefficient cross-field transport ($\varepsilon \lesssim 0.1$), the particles remain confined to their original magnetic channels and are carried away from Earth. Consequently, their observed flux is suppressed despite their relative proximity.

Conversely, sources in the Cygnus region, such as Cyg X-1 [26] and V404 Cygni [27], are magnetically connected to our location. This alignment enhances the observed flux by funneling their cosmic rays toward us, as illustrated in Fig. 1.

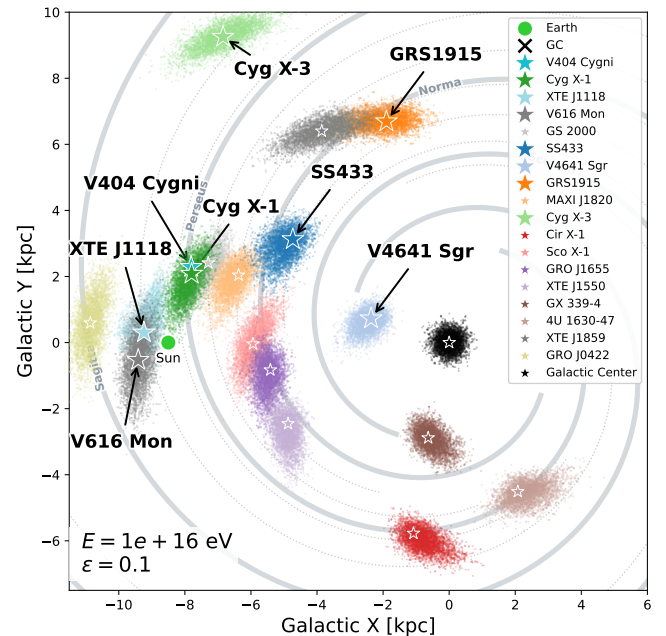


FIG. 1. Illustration of the spatial distribution of 10 PeV cosmic rays (colored dots) from known Galactic microquasar locations (stars). The CR transport is influenced by the filamentary morphology of the Galactic magnetic field (gray spirals). For this comparison, we assume a uniform source age and jet duration of $\tau_{\text{age}} = \tau_{\text{dur}} = 0.2 \text{ Myr}$ with an anisotropy level of $\varepsilon = 0.1$.

To investigate the dominance of GMF architecture over spatial proximity, we compare the predicted flux from the connected Cyg X-1 ($d \approx 2.22 \text{ kpc}$ [26]) with the non-connected V616 Mon ($d \approx 1.06 \text{ kpc}$). For fair comparison, we inject CRs during an assumed jet active phase of 0.2 Myr and normalize the energy budget to the Eddington luminosity of a $10M_{\odot}$ black hole, assuming a CR conversion efficiency of $\eta_{\text{cr}} = 0.005$.

The resulting fluxes in Fig. 2 demonstrate that for an active source, the impact of the anisotropy diffusion parameter ε (dashed versus solid lines) is more significant than the physical distance of the source (blue versus red curves). Because CRs from the non-magnetically-connected source must undergo suppressed diffusive transport in the direction perpendicular to the field lines to reach Earth, the flux from V616 Mon is heavily attenuated. Consequently, a source at the location of Cyg X-1 represents a more viable local candidate to contribute to the observed PeV flux, despite its greater distance. As an active source on a connected GMF line, its flux remains robust even when ε is reduced from 0.1 to 0.01.

The influence of anisotropic diffusion within the GMF becomes even more pronounced for microquasar remnants. Once the central engines are shut off, the observable spatial distribution relies entirely on the magnetic field architecture. This makes a source's position relative to the GMF as vital as its intrinsic power for reproducing

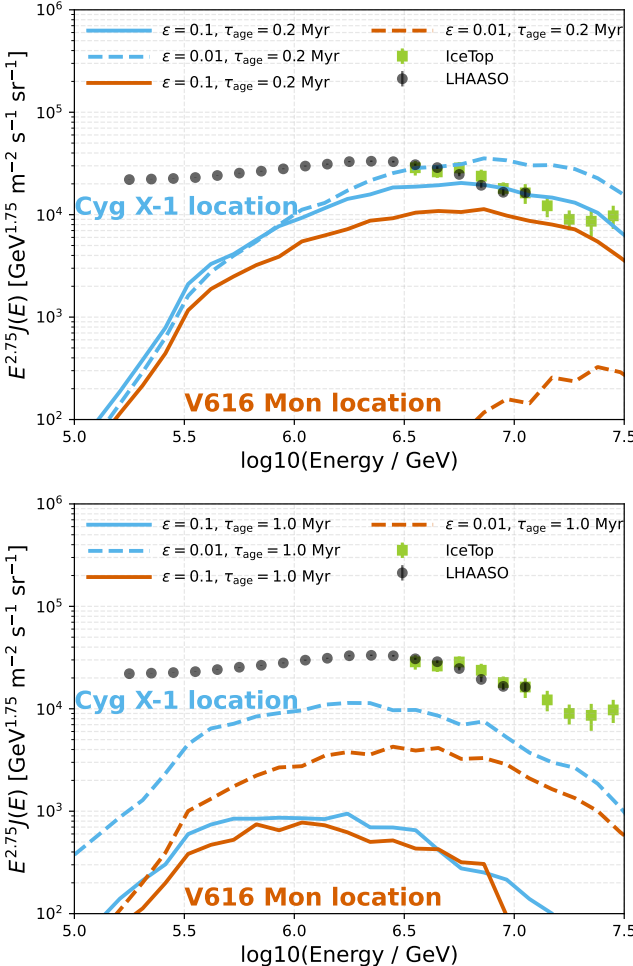


FIG. 2. Predicted CR spectra from Cyg X-1 and V616 Mon locations compared with LHAASO [1] and IceTop [28] data. Results show anisotropic diffusion ($\varepsilon = 0.1, 0.01$) at $\tau_{\text{age}} = 0.2$ Myr (top) and $\tau_{\text{age}} = 1$ Myr (bottom). We assume Model A injection with $M_{\text{BH}} = 10M_{\odot}$, $\tau_{\text{dur}} = 0.2$ Myr, and $\eta_{\text{cr}} = 0.005$.

the “knee,” considering the extended time of CR propagation beyond the lifetime of the engine. Comparing the active and remnant scenarios in the top and bottom panels of Fig. 2 reveals a clear spectral evolution. The active source exhibits a significantly harder spectral feature and a higher flux level, suggesting that active nearby microquasars could potentially create localized spectral features at high energies.

However, the absence of such features above 10 PeV in current observations suggests that particles from currently active sources, such as Cygnus X-1, may still be confined within their local environments. Notably, the distribution around the Galactic Center in Fig. 1 showcases how the GMF ideally confines the escaped PeV CRs. In contrast, CRs from microquasar remnants have had sufficient time to escape their local environments and diffuse through the GMF. This allows them to soften and fill the observed diffuse PeV CR “sea” discussed next.

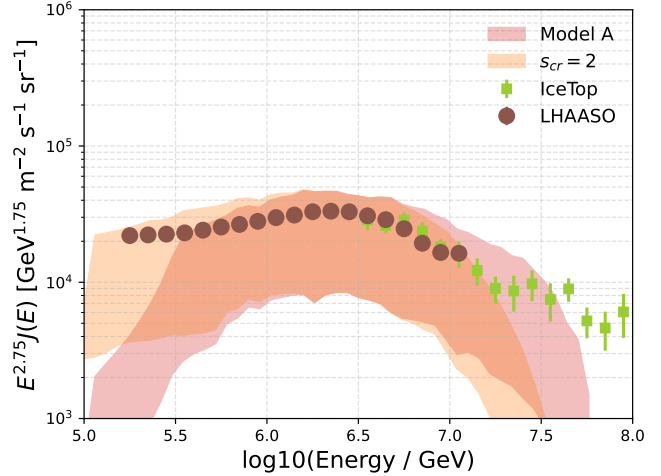


FIG. 3. Diffuse CR energy spectra for Monte Carlo ensembles (shaded bands) of microquasars, assuming an anisotropic diffusion coefficient of $\varepsilon = 0.1$. Each ensemble represents a realization of the Galactic microquasar remnants population. The spectrum from injection Model A (red) with $\eta_{\text{cr}} = 0.005$ is compared against a power-law scenario (orange) characterized by $s_{\text{cr}} = 2$, $E_{\text{max}} = 6$ PeV, and $\eta_{\text{cr}} = 0.03$.

Contributions of Microquasars Remnants— Microquasar remnants provide a non-negligible component of the local CR flux. The time required for PeV CRs to effectively diffuse away from a remnant is governed by the pp interaction rate: $t_{pp}^{-1} \approx (\sigma_{pp}\kappa_{pp}n_{\text{gas}}c) \simeq 0.02 (n_{\text{gas}}/1 \text{ cm}^{-3})/\text{Myr}$. This corresponds to a vast source horizon of $d_H = \sqrt{6D t_{pp}} \sim 60$ kpc, implying that the entire Galactic microquasar population potentially contributes to the local flux. However, CRs must have sufficient time to diffuse to the solar neighborhood after escaping from the remnants. Most distant microquasars may not reach Earth during their short active lifetimes compared to the history of the Milky Way, but they act as primary injectors for the diffuse “sea”, with their remnant clouds continuing to expand and contribute long after the central engines have shut off. Consequently, the local CR environment is shaped by these “remnants”, representing an integrated history of Galactic microquasar activity.

To quantify these contributions, we uniformly sample Galactic microquasars over a 50 Myr history, assuming a constant birth rate $\mathcal{R}_{\text{MQ}} \approx 2 \times 10^{-4} \text{ yr}^{-1}$. Each source is assigned an active lifetime between 0.1 and 1 Myr with a spatial distribution following the radial profile of supernova remnants [29]. For computational efficiency while focusing on sources contributing to the observed CR flux above 100 TeV, the simulation considers microquasars within 0.5 to 5 kpc and with ages up to 5 Myr. The total CR energy budget for each source is $W_{\text{cr}} = \eta_{\text{cr}} L_{\text{Edd}} \tau_{\text{dur}}$, where the accretion-powered luminosity is scaled to the Eddington limit.

The resulting energy spectra, presented in Fig. 3,

demonstrate that this cumulative contribution can account for the observed local CR emission. The uncertainty band reveals possible variance inherent in the stochastic ensembling. This spread highlights that the local PeV CRs are not a simple steady state average, but rather a unique snapshot, unveiling the history and proximity of nearby microquasars' activities. Combined with Fig. 2, we interpret that the present observed local flux may be dominated by a few recent or nearby events. This characterizes the current epoch as a unique snapshot within a dynamic Galactic background.

We compare the Model A scenario with the standard E^{-2} model ($s_{\text{cr}} = 2$, $E_{\text{max}} = 6$ PeV). After normalization, both can reproduce the observed flux, and both remain well below the 10% L_{Edd} threshold typically assumed for jet kinetic power [30]. However, Model A accounts for the observed flux with a CR loading efficiency of only $\eta_{\text{cr}} \approx 0.5\%$, whereas the E^{-2} case demands $\eta_{\text{cr}} \approx 3\%$. This makes Model A more efficient at reproducing the observed PeV CR flux, positioning a less stringent requirement on the energy budget of the jet-driven scenario.

Discussion and Conclusions— The role of microquasars as primary contributors to the observed local PeV CRs is governed by a critical interplay between the injection spectrum, the source age, and the Galactic magnetic field. Our results demonstrate that a hard injection spectrum offers a feasible interpretation for the observed PeV flux while maintaining an energy budget below 1% L_{Edd} . This allows microquasar remnants to reproduce the local PeV CR flux without the stringent requirements on CR loading efficiency imposed by standard power law models.

The age of the source population is equally decisive in satisfying observational constraints. We find that a remnant phase ($\tau_{\text{age}} \approx 1$ Myr) is favored over younger, active scenarios based on the observed flux. While a recent source ($\tau_{\text{age}} \approx 0.2$ Myr) produces an excessive flux in the hard spectrum regime that may conflict with observations, a 1 Myr remnant cloud has diffused sufficiently to remain within allowed levels. Furthermore, our simulations reveal that magnetic connectivity is as influential as intrinsic CR luminosity and age. In highly anisotropic regimes ($\varepsilon = 0.01$), the flux from sources aligned with large-scale field lines, such as Cyg X-1, is significantly enhanced. Conversely, sources like V616 Mon are suppressed by inefficient cross-field transport.

The slow diffusion of CRs in the vicinity of the source is physically possible and primarily relevant when considering the contribution of nearby active microquasars. In the case of microquasar remnants, such confinement effects are less significant since the CRs have already escaped the system. In future studies, the potential confinement of escaped CRs by the local environment surrounding the microquasar, such as the lobes [18], is critical to better understand both active microquasars and recent remnants. Because the history and spatial distribution of microquasars result in distinct observed spectra,

TABLE I. Galactic coordinates and distances for some microquasars, ordered by proximity to the Sun. The Galactic Center is provided for reference.

Source Name	<i>l</i> ($^{\circ}$)	<i>b</i> ($^{\circ}$)	<i>d</i> (kpc)
V616 Mon [24]	210.04	-6.54	1.06
XTE J1118+480 [25]	157.69	+62.31	1.72
Cygnus X-1 [26]	71.33	+3.07	2.22
V404 Cygni [27]	73.12	-2.07	2.39
GRO J0422+32 [33]	165.88	-11.91	2.49
GS 2000+251 [34]	63.37	-3.01	2.70
Scorpius X-1 [35]	359.09	+23.78	2.80
MAXI J1820+070 [36]	43.83	+5.29	2.96
GRO J1655-40 [37]	344.98	+2.46	3.20
4U 1755-33 [38]	357.22	-4.87	4.00
CI Cam [39]	148.47	+4.26	4.10
XTE J1550-564 [40]	325.88	-1.84	4.38
SS 433 [41]	39.70	-2.20	4.90
V4641 Sgr [42]	6.77	-4.79	6.20
XTE J1859+226 [43]	54.05	+8.61	8.00
GX 339-4 [44]	339.86	-4.32	8.40
<i>Galactic Center</i>	0.00	0.00	8.50
GRS 1915+105 [45, 46]	45.40	-0.20	9.40
Cygnus X-3 [47]	79.85	+0.68	9.40
Circinus X-1 [48]	322.12	-0.03	9.40
4U 1630-47 [49]	336.91	+0.25	11.50

a complete all-sky sample from future ultra-high-energy gamma-ray facilities will be essential to definitively establish them as Galactic PeVatrons [9, 31, 32].

Our findings imply that a comprehensive understanding of the spatial distribution and particle escape processes of microquasars is essential to resolving their role in shaping the observed CR spectrum around the “knee”. Comparison to observed anisotropy can further constrain the favored parameter range; however, we leave this for future work as it remains challenging due to computational limitations in simulating the high statistics required at the solar neighborhood.

In summary, the local CR environment is dominated by the accumulated output of microquasar remnants. The PeV sky is therefore a signature of the integrated history of the Galaxy, where the contributions of ancient jets persist long after their central engines have ceased.

Appendix A

Table I summarizes the spatial parameters of the observed microquasars used to generate the map in Fig. 1.

The parameter space illustrated in Fig. 4 quantifies the conditions under which an individual source might dominate the local PeV flux. The central contours indicate that dominance is restricted to nearby, recently active sources ($d \lesssim 0.5$ kpc, $\tau_{\text{age}} \lesssim 0.2$ Myr). At greater distances ($d \sim 2$ kpc), the contribution falls by nearly an order of magnitude. These results contextualize the values for known objects like Cygnus X-1, which has a dis-

tance $d = 2.22$ kpc [26] and an estimated jet duration of 0.04 to 0.3 Myr [30]. While such sources contribute minimally under the assumption of isotropic diffusion without GMF, their role is significantly modulated when accounting for the magnetic field.

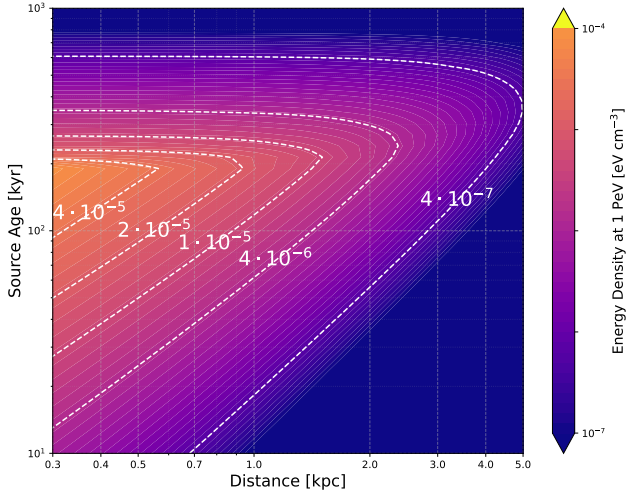


FIG. 4. Cosmic ray energy density at 1 PeV shown as a function of distance and source age. The model assumes a jet duration $\tau_{\text{dur}} = 0.2$ Myr from a $10M_{\odot}$ black hole and isotropic diffusion without GMF effects. The injection spectrum $Q(E)$ is normalized such that the total cosmic ray luminosity is $L_{\text{cr}} = \eta_{\text{cr}} L_{\text{Edd}}$, where we adopt $\eta_{\text{cr}} = 0.1$. The spectral index is assumed to be $s_{\text{cr}} = 2$. Contours identify density levels between 4×10^{-7} and 4×10^{-5} eV cm $^{-3}$.

[1] Z. Cao *et al.* (LHAASO), First Identification and Precise Spectral Measurement of the Proton Component in the Cosmic-Ray ‘Knee’, [arXiv:2505.14447 \[astro-ph.HE\]](https://arxiv.org/abs/2505.14447) (2025).

[2] Z. Cao *et al.* (LHAASO), Measurements of All-Particle Energy Spectrum and Mean Logarithmic Mass of Cosmic Rays from 0.3 to 30 PeV with LHAASO-KM2A, *Phys. Rev. Lett.* **132**, 131002 (2024), [arXiv:2403.10010 \[astro-ph.HE\]](https://arxiv.org/abs/2403.10010).

[3] Z. Cao *et al.* (LHAASO), Precise Measurement of Cosmic Ray Light and Helium Spectra above 0.1 Peta-electron-Volt, [arXiv:2511.05013 \[astro-ph.HE\]](https://arxiv.org/abs/2511.05013) (2025).

[4] B. T. Zhang, S. S. Kimura, and K. Murase, Microquasar jet-cocoon systems as PeVatrons, *Phys. Rev. D* **112**, 123015 (2025), [arXiv:2506.20193 \[astro-ph.HE\]](https://arxiv.org/abs/2506.20193).

[5] H. Yue, L. Nie, Y.-Q. Guo, and H.-B. Hu, Joint constraint on the propagation origin of the cosmic-ray spectral knee from energy spectrum and anisotropy observations, [arXiv:2601.17851 \[astro-ph.HE\]](https://arxiv.org/abs/2601.17851) (2026).

[6] J. Wang, B. Reville, and F. A. Aharonian, Galactic Superaccreting X-Ray Binaries as Super-PeVatron Accelerators, *Astrophys. J. Lett.* **989**, L25 (2025), [arXiv:2507.21048 \[astro-ph.HE\]](https://arxiv.org/abs/2507.21048).

[7] S. Kaci, G. Giacinti, F. Aharonian, and J.-S. Wang, Mi- croquasars as the major contributors to Galactic cosmic rays around the “knee”, [arXiv:2510.01369 \[astro-ph.HE\]](https://arxiv.org/abs/2510.01369) (2025).

[8] K. Fang and F. Halzen, The Cosmic-ray Knee as a Local Signature of Nearby PeVatrons, [arXiv:2601.05435 \[astro-ph.HE\]](https://arxiv.org/abs/2601.05435) (2026).

[9] The LHAASO Collaboration, Z. Cao, F. Aharonian, Y.-X. Bai, Y.-W. Bao, D. Bastieri, X.-J. Bi, Y.-J. Bi, W.-Y. Bian, A. V. Bukevich, C. Cai, W.-Y. Cao, Z. Cao, J. Chang, J.-F. Chang, A. Chen, E.-S. Chen, G. Chen, H.-X. Chen, L. Chen, L. Chen, M.-J. Chen, M.-L. Chen, Q.-H. Chen, S. Chen, S.-H. Chen, S.-Z. Chen, T.-L. Chen, X.-B. Chen, X. Chen, Y. Chen, N. Cheng, Y.-D. Cheng, M. Chung Chu, M.-Y. Cui, S.-W. Cui, X.-H. Cui, Y.-D. Cui, B.-Z. Dai, H.-L. Dai, Z. Dai, D. Luobu, Y.-X. Diao, X.-Q. Dong, K.-K. Duan, J.-H. Fan, Y.-Z. Fan, J. Fang, J.-H. Fang, K. Fang, C.-f. Feng, H. Feng, L. Feng, S. Feng, X.-t. Feng, Y. Feng, Y.-l. Feng, S. Gabici, B. Gao, C.-d. Gao, Q. Gao, W. Gao, W.-k. Gao, M. Ge, T.-T. Ge, L. Geng, G. Giacinti, G. Gong, Q. Gou, M.-H. Gu, F.-L. Guo, J. Guo, X.-L. Guo, Y.-Q. Guo, Y.-Y. Guo, Y.-A. Han, O. A. Hannuksela, M. Hasan, H.-H. He, H.-N. He, J.-Y. He, X. He, Y. He, S. Hernández-Cadena, B.-W. Hou, C. Hou, X. Hou, H.-B. Hu, S.-C. Hu, C. Huang, D.-

H. Huang, J. Huang, T.-Q. Huang, W.-J. Huang, X.-T. Huang, X.-Y. Huang, Y. Huang, Y.-Y. Huang, X.-L. Ji, H.-Y. Jia, K. Jia, H.-B. Jiang, K. Jiang, X.-W. Jiang, Z.-J. Jiang, M. Jin, S. Kaci, M.-M. Kang, I. Karpikov, D. Khangulyan, D. Kuleshov, K. Kurinov, B.-B. Li, C. Li, C. Li, D. Li, F. Li, H. Li, H. Li, J. Li, J. Li, K. Li, L. Li, R.-L. Li, S.-D. Li, T.-Y. Li, W.-L. Li, X.-R. Li, X. Li, Y. Li, Y. Li, Z. Li, Z. Li, E.-W. Liang, Y.-F. Liang, S.-J. Lin, B. Liu, C. Liu, D. Liu, D.-B. Liu, H. Liu, H.-D. Liu, J. Liu, J.-L. Liu, J.-R. Liu, M.-Y. Liu, R.-Y. Liu, S.-M. Liu, W. Liu, X. Liu, Y. Liu, Y. Liu, Y.-N. Liu, Y.-Q. Lou, Q. Luo, Y. Luo, H.-K. Lv, B.-Q. Ma, L.-L. Ma, X.-H. Ma, J.-R. Mao, Z. Min, W. Mitthumsiri, G.-B. Mou, H.-J. Mu, A. Neronov, K. C. Y. NG, M.-Y. Ni, L. Nie, L.-J. Ou, P. Pattarakijwanich, Z.-Y. Pei, J.-C. Qi, M.-Y. Qi, J.-J. Qin, A. Raza, C.-Y. Ren, D. Ruffolo, A. Sáiz, D. Semikoz, L. Shao, O. Shchegolev, Y.-Z. Shen, X.-D. Sheng, Z. Shi, F.-W. Shu, H.-C. Song, Y. V. Stenkin, V. Stepanov, Y. Su, D. Sun, H. Sun, Q. Sun, X. Sun, Z. Sun, N. Hussain Tabasam, J. Takata, P. H. T. Tam, H.-B. Tan, and Q. Tang, Ultrahigh-Energy Gamma-ray Emission Associated with Black Hole-Jet Systems, [arXiv e-prints](#), [arXiv:2410.08988](#) (2024), [arXiv:2410.08988](#) [astro-ph.HE].

[10] Z. Cao *et al.* (LHAASO), Cygnus X-3: A variable peta-electronvolt gamma-ray source, [arXiv:2512.16638](#) [astro-ph.HE] (2025), [arXiv:2512.16638](#).

[11] L. Abaroa, G. E. Romero, and V. Bosch-Ramon, Microquasar remnants as hidden PeVatrons, [Astron. Astrophys. **705**, L4](#) (2026), [arXiv:2512.07781](#) [astro-ph.HE].

[12] L. Merten, J. Becker Tjus, H. Fichtner, B. Eichmann, and G. Sigl (CRPropa), CRPropa 3.1—a low energy extension based on stochastic differential equations, [JCAP **06**, 046](#), [arXiv:1704.07484](#) [astro-ph.IM].

[13] A. AL-Zetoun, Propagation of Galactic cosmic rays: the influence of anisotropic diffusion, [arXiv:2506.13314](#) [astro-ph.HE] (2025).

[14] A. Neronov, F. Oikonomou, and D. Semikoz, Multimesenger signature of cosmic rays from the microquasar V4641 Sgr propagating along a Galactic magnetic field line, [Phys. Rev. D **111**, 103025](#) (2025), [arXiv:2410.17608](#) [astro-ph.HE].

[15] R. Jansson and G. R. Farrar, The Galactic Magnetic Field, [Astrophys. J. Lett. **761**, L11](#) (2012), [arXiv:1210.7820](#) [astro-ph.GA].

[16] J. Kleimann, T. Schorlepp, L. Merten, and J. Becker Tjus, Solenoidal Improvements for the JF12 Galactic Magnetic Field Model, [Astrophys. J. **877**, 76](#) (2019), [arXiv:1809.07528](#) [astro-ph.GA].

[17] R. P. Fender and G. G. Pooley, Infrared synchrotron oscillations in grs 1915+105, [Mon. Not. Roy. Astron. Soc. **300**, 573](#) (1998), [arXiv:astro-ph/9806073](#).

[18] V. Bosch-Ramon, M. Perucho, and P. Bordas, The termination region of high-mass microquasar jets, [Astron. Astrophys. **528**, A89](#) (2011), [arXiv:1101.5049](#) [astro-ph.HE].

[19] G. Giacinti, M. Kachelriess, and D. V. Semikoz, Reconciling cosmic ray diffusion with Galactic magnetic field models, [JCAP **07**, 051](#), [arXiv:1710.08205](#) [astro-ph.HE].

[20] F. Casse, M. Lemoine, and G. Pelletier, Transport of cosmic rays in chaotic magnetic fields, [Phys. Rev. D **65**, 023002](#) (2002), [arXiv:astro-ph/0109223](#).

[21] P. Reichherzer, J. Becker Tjus, E. G. Zweibel, L. Merten, and M. J. Pueschel, Turbulence-Level Dependence of Cosmic-Ray Parallel Diffusion, [Mon. Not. Roy. Astron. Soc. **498**, 5051](#) (2020), [arXiv:1910.07528](#) [astro-ph.HE].

[22] P. Blasi, The Origin of Galactic Cosmic Rays, [Astron. Astrophys. Rev. **21**, 70](#) (2013), [arXiv:1311.7346](#) [astro-ph.HE].

[23] R. Jansson and G. R. Farrar, A New Model of the Galactic Magnetic Field, [Astrophys. J. **757**, 14](#) (2012), [arXiv:1204.3662](#) [astro-ph.GA].

[24] T. E. Harrison, S. B. Howell, P. Szkody, and F. A. Cordero, The Nature of the Secondary Star in the Black Hole X-Ray Transient V616 Mon (=A0620-00), [Astron. J. **133**, 162](#) (2007), [arXiv:astro-ph/0609535](#).

[25] D. M. Gelino, S. Balman, U. Kizilouglu, A. Yilmaz, E. Kalemci, and J. A. Tomsick, The inclination angle of and mass of the black hole in xte j1118+480, [Astrophys. J. **642**, 438](#) (2006), [arXiv:astro-ph/0601409](#).

[26] J. C. A. Miller-Jones *et al.*, Cygnus X-1 contains a 21-solar mass black hole—Implications for massive star winds, [Science **371**, 1046](#) (2021), [arXiv:2102.09091](#) [astro-ph.HE].

[27] J. C. A. Miller-Jones, P. G. Jonker, V. Dhawan, W. Brisken, M. P. Rupen, G. Nelemans, and E. Gallo, The First Accurate Parallax Distance to a Black Hole, [Astrophys. J. Lett. **706**, L230](#) (2009), [arXiv:0910.5253](#) [astro-ph.HE].

[28] M. G. Aartsen *et al.* (IceCube), Cosmic ray spectrum and composition from PeV to EeV using 3 years of data from IceTop and IceCube, [Phys. Rev. D **100**, 082002](#) (2019), [arXiv:1906.04317](#) [astro-ph.HE].

[29] D. A. Green, Constraints on the distribution of supernova remnants with Galactocentric radius, [Mon. Not. R. Astron. Soc. **454**, 1517](#) (2015), [arXiv:1508.02931](#) [astro-ph.HE].

[30] E. Gallo, R. Fender, C. Kaiser, D. Russell, R. Morganti, T. Oosterloo, and S. Heinz, A dark jet dominates the power output of the stellar black hole Cygnus X-1, [Nature \(London\) **436**, 819](#) (2005), [arXiv:astro-ph/0508228](#) [astro-ph].

[31] F. Aharonian *et al.* (H.E.S.S.), Acceleration and transport of relativistic electrons in the jets of the microquasar SS 433, [Science **383**, adi2048](#) (2024), [arXiv:2401.16019](#) [astro-ph.HE].

[32] P. Abreu *et al.* (SWGO), Science Prospects for the Southern Wide-field Gamma-ray Observatory: SWGO, [arXiv:2506.01786](#) [astro-ph.HE] (2025).

[33] D. M. Gelino and T. E. Harrison, Gro j0422+32: the lowest mass black hole?, [Astrophys. J. **599**, 1254](#) (2003), [arXiv:astro-ph/0308490](#).

[34] P. J. Callanan, M. R. Garcia, A. V. Filippenko, I. McLean, and H. Teplitz, On the Mass of the Black Hole in GS 2000+25, [Astrophys. J. Lett. **470**, L57](#) (1996).

[35] C. F. Bradshaw, E. B. Fomalont, and B. J. Geldzahler, High-Resolution Parallax Measurements of Scorpius X-1, [Astrophys. J. Lett. **512**, L121](#) (1999).

[36] P. Atri *et al.*, A radio parallax to the black hole X-ray binary MAXI J1820+070, [Mon. Not. Roy. Astron. Soc. **493**, L81](#) (2020), [arXiv:1912.04525](#) [astro-ph.HE].

[37] R. M. Hjellming and M. P. Rupen, Episodic Ejection of Relativistic Jets by the X-Ray Transient GRO:J1655-40, [Nature **375**, 464](#) (1995).

[38] L. Angelini and N. E. White, An XMM-Newton observation of 4U1755-33 in quiescence: Evidence for a fossil x-ray jet, [Astrophys. J. Lett. **586**, L71](#) (2003), [arXiv:astro-ph/0302315](#).

[39] E. A. Barsukova, A. N. Burenkov, V. P. Goranskij, S. V. Zharikov, L. Iliev, N. Manset, N. V. Metlova, A. S. Miroshnichenko, A. V. Moiseeva, P. L. Nedialkov, E. A. Semenko, K. Stoyanov, and I. A. Yakunin, B[e] Star CI Camelopardalis in the Optical Range, *Astrophysical Bulletin* **78**, 1 (2023), arXiv:2412.12305 [astro-ph.SR].

[40] G. Migliori, S. Corbel, J. A. Tomsick, P. Kaaret, R. P. Fender, T. Tzioumis, M. Coriat, and J. A. Orosz, Evolving morphology of the large-scale relativistic jets from XTE J1550–564, *Mon. Not. Roy. Astron. Soc.* **472**, 141 (2017), arXiv:1707.06876 [astro-ph.HE].

[41] Y. Su, X. Zhou, J. Yang, Y. Chen, X. Chen, and S. Zhang, The Large-scale Interstellar Medium of SS 433/W50 Revisited, *Astrophys. J.* **863**, 103 (2018), arXiv:1807.03737 [astro-ph.GA].

[42] R. K. D. MacDonald, C. D. Bailyn, M. Buxton, A. G. Cantrell, R. Chatterjee, R. Kennedy-Shaffer, J. A. Orosz, C. B. Markwardt, and J. H. Swank, The Black Hole Binary V4641 Sagitarii: Activity in Quiescence and Improved Mass Determinations, *Astrophys. J.* **784**, 2 (2014), arXiv:1401.4190 [astro-ph.SR].

[43] R. I. Hynes, The Optical and Ultraviolet Spectral Energy Distributions of Short-Period Black Hole X-Ray Transients in Outburst, *Astrophys. J.* **623**, 1026 (2005), arXiv:astro-ph/0412531 [astro-ph].

[44] M. L. Parker *et al.*, NuSTAR and Swift observations of the very high state in GX 339-4: Weighing the black hole with X-rays, *Astrophys. J. Lett.* **821**, L6 (2016), arXiv:1603.03777 [astro-ph.HE].

[45] J. Inokuchi, K. S. Kawabata, M. Uemura, and H. Hiraga, Polarimetric Study of GRS 1915+105: Estimation of Interstellar Polarization Component, arXiv:2501.02835 [astro-ph.IM] (2025).

[46] M. Reid and J. Miller-Jones, On the distances to the x-ray binaries cygnus x-3 and grs 1915+ 105, *The Astrophysical Journal* **959**, 85 (2023).

[47] M. J. Reid and J. C. A. Miller-Jones, On the Distances to the X-Ray Binaries Cygnus X-3 and GRS 1915+105, *Astrophys. J.* **959**, 85 (2023), arXiv:2309.15027 [astro-ph.HE].

[48] S. Heinz, M. G. Burton, C. Braiding, W. N. Brandt, P. G. Jonker, P. Sell, R. P. Fender, M. A. Nowak, and N. S. Schulz, Lord of the Rings: A Kinematic Distance to Circinus X-1 from a Giant X-Ray Light Echo, *Astrophys. J.* **806**, 265 (2015), arXiv:1506.06142 [astro-ph.HE].

[49] E. Kalemci, T. J. Maccarone, and J. A. Tomsick, A Dust-scattering Halo of 4U 1630–47 Observed with Chandra and Swift: New Constraints on the Source Distance, *Astrophys. J.* **859**, 88 (2018), arXiv:1804.02909 [astro-ph.HE].